UC San Diego
UC San Diego Previously Published Works

Title

Optical edge detection based on high-efficiency dielectric metasurface

Permalink

Journal

ISSN

Authors

Zhou, Junxiao
Qian, Haoliang
Chen, Ching-Fu
et al.

Publication Date

DOI

Peer reviewed

Optical edge detection based on high-efficiency dielectric metasurface

Junxiao Zhou[a,b,1], Haoliang Qian[b,1], Ching-Fu Chen[b], Junxiang Zhao[b], Guangru Li[b], Qianyi Wu[b], Hailu Luo[a,2], Shuangchun Wen[a], and Zhaowei Liu[b,2]

[a]Key Laboratory for Micro-/Nano-Optoelectronic Devices of Ministry of Education, School of Physics and Electronics, Hunan University, 410082 Changsha, China; and [b]Department of Electrical and Computer Engineering, University of California, San Diego, La Jolla, CA 92093

Optical edge detection is a useful method for characterizing boundaries, which is also in the forefront of image processing for object detection. As the field of metamaterials and metasurface is growing fast in an effort to miniaturize optical devices at unprecedented scales, experimental realization of optical edge detection with metamaterials remains a challenge and lags behind theoretical proposals. Here, we propose a mechanism of edge detection based on a Pancharatnam–Berry-phase metasurface. We experimentally demonstrated broadband edge detection using designed dielectric metasurfaces with high optical efficiency. The metasurfaces were fabricated by scanning a focused laser beam inside glass substrate and can be easily integrated with traditional optical components. The proposed edge-detection mechanism may find important applications in image processing, high-contrast microscopy, and real-time object detection on compact optical platforms such as mobile phones and smart cameras.

edge detection | spatial differentiation | metasurface | Pancharatnam–Berry phase

Edge detection is the first step of human visual perception and is fundamentally important in the human visual system (1). Edge detection significantly reduces the amount of data to be processed, since it extracts meaningful information and preserves important geometric features. To detect the edges of an object, the object information is processed by either digital computation or analog computation. In practice, as an optical analog computation element, spatial differentiator enables massively parallel processing of edge detection from an entire image, which offers advantages over digital computation: It can deal with real-time and continuous image processing with high speed and is power-saving in specialized computational tasks (2–4).

During the past few years, optical metamaterials and metasurfaces have been suggested to perform analog spatial differentiation for edge detection (5–17) which show superior integration capability compared with the traditional bulky system comprising lenses and spatial filters (18). A suitably designed metamaterial structure was theoretically proposed to perform desired mathematical operations including edge detection as light propagates through it (6). Deliberately designed layered structure was also suggested for spatial differentiation when an incident beam is reflected from it (8–10). Plasmonic dark-field microscopy utilizes near-field surface plasmon waves to excite the object, and can be also treated as an efficient approach for edge detection (16). However, to the best of our knowledge, free-space broadband edge detection has not been reported yet because either the system can only be applied for surface imaging (16, 19) or the fabrication involved is too complicated (6, 8–10, 13).

Here, we propose a mechanism to implement an optical spatial differentiator consisting of a designed Pancharatnam–Berry (PB)-phase metasurface inserted between two orthogonally aligned linear polarizers (20–22). Unlike other spatial differentiator approaches, our method does not depend on complex layered structures or critical plasmonic coupling condition, but instead is based on spin-to-orbit interactions. Experiment confirms

that broadband optical analog computing enables the edge detection of an object and achieves tunable resolution at the resultant edges. Furthermore, metasurface orientation-dependent edge detection is also demonstrated experimentally.

Concept of Edge-Detection Metasurface

Metasurface has been widely used for splitting the left-handed and right-handed circularly polarized (LCP and RCP) beam to different directions (23–29). Especially, PB phase metasurface is a popular candidate due to its robust and lower recline on precision fabrication. A typical example is illustrated in Fig. 1A, when a linear-polarized plane wave is incident on a PB phase gradient metasurface with phase $\varphi(x,y) = \frac{\pi x}{\Lambda}$ (assuming the phase gradient direction is along x axis with period of Λ), the LCP and RCP components gain additional phase $+2\varphi$ and -2φ (Fig. 1B), respectively. To explain the edge-detection concept of this work, a square-shaped object is illuminated by a linearly polarized (LP) light along x direction. Its electric field distribution can be written as $E_{in}(x,y)$ (Fig. 1E) at object/image plane and $\tilde{E}(u,v)$ at Fourier plane (Fig. 1C for the magnitude spectrum). If we introduce a PB phase gradient metasurface at the Fourier plane

Fig. 1. The proposed concept of edge detection based on a designed phase gradient metasurface. (*A*) When PB phase gradient metasurface is illuminated by collimated LP beam, two separated LCP and RCP beam components are observed. (*B*) Resultant phase gradient of LCP and RCP component. The Fourier space spectrum (*C*) and real-space image (*E*) of a square object. *C* and *E* will be changed to *D* and *F*, respectively, when a PB phase gradient metasurface is added at the Fourier plane. Blue- and red-shaded areas indicate the resultant edge information along the PB phase gradient direction.

(Fig. 1*D*), the output electrical field at image plane can be given as (*SI Appendix, Detailed Formulations*)

$$E_{out}(x,y) = E_{in}[(x-\Delta),y]\begin{bmatrix} 1 \\ -i \end{bmatrix} + E_{in}[(x+\Delta),y]\begin{bmatrix} 1 \\ i \end{bmatrix}. \quad [1]$$

This means that the LCP and RCP component possesses opposite phase gradient, which leads the LCP and RCP images translating a distance of $\Delta = \frac{\lambda f}{\Lambda}$ but with opposite directions (Fig. 1*F*). Here, λ is the working wavelength and f is the focus length. If an analyzer (orthogonal linear polarizer along y direction) is employed upon the images shown in Fig. 1*F*, it is apparent that only the two shaded areas can go through, indicating the edge-detection function. The final electrical field goes through the whole system and could be rewritten as

$$E_{out\_edge}(x,y) = (E_{in}[(x+\Delta),y] - E_{in}[(x-\Delta),y])\begin{bmatrix} 0 \\ i \end{bmatrix}. \quad [2]$$

If the shift Δ is much smaller than the image profile, $E_{out\_edge}(x,y)$ is approximately proportional to the first-order spatial differentiation of the input $E_{in}(x,y)$:

$$E_{out\_edge}(x,y) \simeq 2\Delta \frac{dE_{in}(x,y)}{d(x)}. \quad [3]$$

Therefore, the proposed edge-detection mechanism can be briefly explained as follows: illuminate an object by linear polarized light and propagate through the metasurface. The left- and right-handed photons with the opposite spin angular momentum acquire opposite extrinsic orbit angular momentum by interacting with the metasurface, as indicated in Eq. **1**, which manifests LCP and RCP images with a tiny shift at the image plane. The overlapped LCP and RCP components recombined to LP thus will be eliminated by the analyzer, leaving out only the edge information available for detection.

Sample Fabrication and Characterization

As shown in Fig. 2*A*, the sample is made of form-birefringent nanostructured glass slabs. The diameter of the glass substrate is 2.5 cm, the thickness is 3 mm, and the pattern area of the sample is 8 mm by 8 mm. The metasurface pattern is fabricated by a femtosecond pulse laser inside of glass, 50 μm beneath the surface. Under intense laser irradiation, a plasma of high free-electron density is generated by a multiphoton ionization process. The interference between the plasma and the incident light beam leads to the stripe-like nanostructure as reported (30). By carefully controlling the polarization of incident beam, the desired orientation of the nanostructure, which is perpendicular to this polarization, can be obtained. More fabrication details could be found in our previous work (31).

We utilized the polariscopy method to demonstrate the local optical slow-axis orientation of this birefringent structure (32). As shown in Fig. 2*B*, crossed linear polarizer imaging under 80× magnification emphasizes the transverse gradient pattern of the optical axis, which corresponds to the dotted square area in Fig. 2*A*. We can clearly see the local orientation of the microscopic structures, i.e., the slow-axis distribution $\varphi(x,y)$ of laser-induced form birefringence. The red bars indicate the orientation of the slow axis over one period of this sample. The nanostructures are on the order of 30~100 nm, as indicated from the scanning electron microscope (SEM) image in Fig. 2*B*, *Inset*. The structure dimension is much smaller than the working wavelength, therefore we can treat it as a birefringence medium with spatially variant optical slow axis. When the light beam passes through the designed inhomogeneous birefringent medium with locally varying optical axis orientations and homogeneous retardation, it will acquire a spatially varying PB phase (33, 34).

Edge-Detection Experiment

We perform a series of experiments to demonstrate versatile edge-detection capabilities. In the first experiment, we use a photolithography fabricated University of California, San Diego (UCSD) library logo (*SI Appendix, Test Object Fabrication* and Fig. S1) to test the edge-detection performance at various working wavelengths. The detailed experimental setup is provided in the experiment setup in (*SI Appendix*, Fig. S2). A 4f system consists of two identical lenses, which are 2f apart from each other. The metasurface is placed at one focal length behind
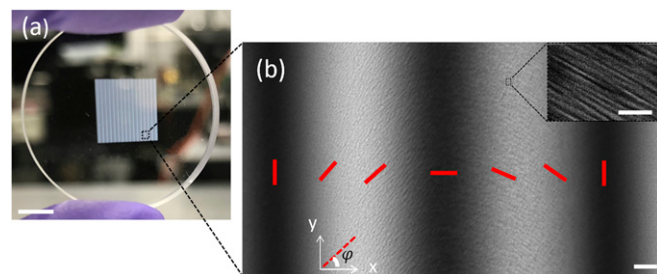

Fig. 2. The metasurface embedded in glass. (*A*) Photograph of a 1-inch-diameter sample. Metasurface patterned area, 8 mm × 8 mm. (Scale bar, 5 mm.) (*B*) Polariscope optical image of the sample pattern area marked in *A*. (Scale bar, 25 μm.) The red bars indicate structures orientation in one period. (*Inset*) SEM image of the induced nanostructure. (Scale bar, 500 nm.)
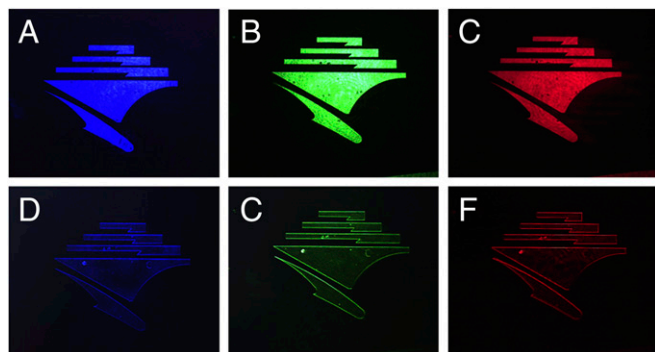
Fig. 3. Broadband edge-detection demonstration. (*A*–*C*) The first row shows images without the analyzer; the illumination wavelengths are 430, 500, and 670 nm, respectively. The images are taken with metasurface period Λ of 8,000 μm. (*D*–*F*) The second row shows resultant images after adding an analyzer.

the first lens and one focal length in front of the second lens. The first lens yields the Fourier transform of the object at its back focal plane, which is exactly the position of the metasurface. In turn, the second lens performs another Fourier transform, delivering a duplicate of the object. When the light passes through the 4f system, we obtain two vertically shifted LCP and RCP images with overlapping area being linear-polarized as shown in Fig. 3 *A*–*C*. The amount of shift of the two images is difficult to see due to the small phase gradient of the metasurface. To block the overlapping area while preserving circularly polarized edge, we put an analyzer after the metasurface so that only the edges can go through, as displayed in Fig. 3 *D*–*F*. The wavelengths are chosen as 430, 500, and 670 nm, which not only confirms the proposed concept of edge detection, but also demonstrates its broadband capability. The broadband property of our metasurface originates from the geometric phase of the nanostructure orientation, which is intrinsically independent of wavelength (31). Additionally, the transfer function of the whole edge-detection system is experimentally measured and provided in
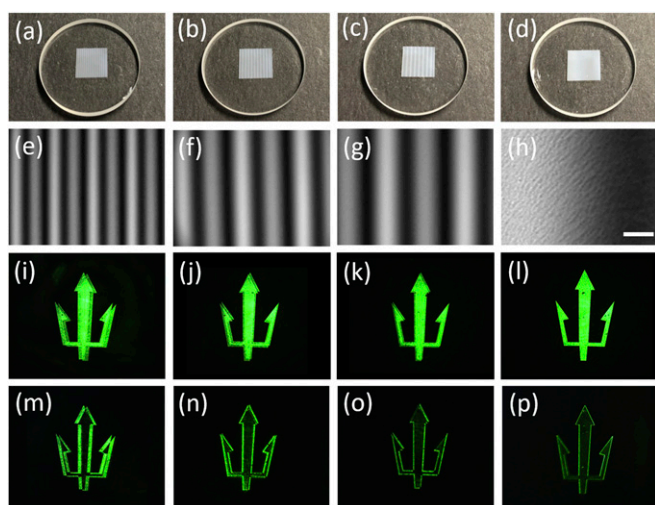
Fig. 4. Edge detection with various resolutions at the wavelength of 500 nm. (*A*–*D*) Photographs of the metasurface sample with different phase gradient periods: 500, 750, 1,000, and 8,000 μm, respectively. (*E*–*H*) Polariscopy images of the samples in the first row. (Scale bar, 125 μm.) (*I*–*L*) Two separated LCP and RCP images without the analyzer. (*M*–*P*) Edge image of different samples corresponding to different resolutions.
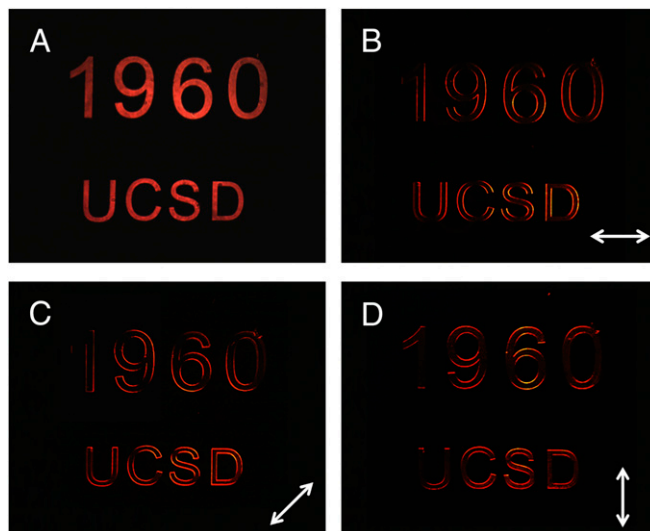
Fig. 5. Orientation-dependent edge detection. (*A*) Original image without edge detection. (*B*–*D*) Different portion of the edge shows up for different metasurface orientations. Arrows indicate the edge-detection direction.

which shows a typical response for the edge-detection function (16).

Additionally, we demonstrate the tunable resolution of the edge images corresponding to different PB phase gradient period Λ. For this experiment, we choose the UCSD Triton insignia as our object (). Fig. 4 *A*–*D* shows the photos of four metasurfaces with Λ equal to 500, 750, 1,000, and 8,000 μm. Fig. 4 *E*–*H* corresponds to the polariscope optical image of the metasurfaces of the first row, which shows different numbers of period within the same field of view (∼2,000 μm). Similar to Fig. 3, without the analyzer, we can see clearly two horizontally shifted LCP and RCP images, as shown in Fig. 4 *I*–*L*. The separation between two images determines how sharp the edge can be resolved, which is also confirmed by the final edge-detection images shown in Fig. 4 *M*–*P*. The highest resolution achieved is around 2 μm (Fig. 4*P*), close to the diffraction limit of the optical system, by using a metasurface with Λ of 8,000 μm. It is worth to note here that these results are taken under the condition of a planar object at the focal plane. Therefore, for thick 3D object, multiple measurements need to be taken by scanning the focal plane over the objects and combine each focal plane result together. In the case of the samples with circular birefringence inclusions, the LCP and RCP components will gain different phases, so that the combined LP components in the overlapped area may not be completely canceled out after the second linear polarizer. Although this indicates the contrast between the edge and the background will be compromised, additional circular birefringence information can be revealed.

We also studied the orientation-dependent edge detection. As shown in Fig. 5*A*, an image of "1960 UCSD" without using the analyzer is represented. Fig. 5 *B*–*D* shows the edge images after the analyzer with different orientations of the metasurface. As we expected, the one-dimensional phase gradient metasurface only provides the sensitivity to the edges along the gradient direction, indicated by the white arrows. The metasurface design can be easily extended to 2D edge detection by changing the one-dimensional phase gradient $\varphi(x,y) = \frac{\pi x}{\Lambda}$ to a radial phase gradient $\varphi(x,y) = \frac{\pi\sqrt{x^2+y^2}}{\Lambda}$. As numerically shown in for 2D edge detection, all edges are clearly revealed.

Conclusions

Edge detection is typically the first step of the subsequent processing stages and its signal might be very weak in many practical scenarios. The optical efficiency of the metasurface, therefore, becomes a critical issue. The optical efficiency of our metasurface is defined as $\eta = \frac{P_{LCP} + P_{RCP}}{P_{INPUT}}$, which can reach around 90% in our experiments. This high efficiency is attributed to the relatively thick glass-based metastructure with high transmission coefficient, showing clear advantages compared with metallic metasurfaces for transmission mode applications. The demonstrated edge-detection scheme is not limited to the birefringence dielectric metasurface but can be implemented by any other PB phase gradient metasurfaces with high optical efficiency (27).

In conclusion, we have proposed, fabricated, and experimentally verified that a PB phase gradient metasurface sandwiched by two orthogonal linear polarizers can be used for broadband optical edge detection with tunable resolution. Although only one-dimensional edge detection is demonstrated in our concept-proof experiment, there are no limitations to extend it to 2D which could be done in the future. Since the edge detection here is enabled by the interplay between different polarization components of light, we envision the PB phase gradient metasurfaces may lead to important applications in polarization-dependent high-contrast microscopy and compact optical processing systems (35).

1. D. H. Hubel, T. N. Wiesel, Receptive fields, binocular interaction and functional architecture in the cat's visual cortex. *J. Physiol.* **160**, 106–154 (1962).
2. C. Goodman The digital revolution: Art in the computer age. *Art J.* **49**, 248–252 (1990).
3. D. R. Solli, B. Jalali, Analog optical computing. *Nat. Photonics* **9**, 704–706 (2015).
4. H. J. Caulfield, S. Dolev, Why future supercomputing requires optics. *Nat. Photonics* **4**, 261–263 (2010).
5. M. Farmahini-Farahani, J. Cheng, H. Mosallaei, Metasurfaces nanoantennas for light processing. *J. Opt. Soc. Am. B* **30**, 2365–2370 (2013).
6. A. Silva *et al.*, Performing mathematical operations with metamaterials. *Science* **343**, 160–163 (2014).
7. A. Pors, M. G. Nielsen, S. I. Bozhevolnyi, Analog computing using reflective plasmonic metasurfaces. *Nano Lett.* **15**, 791–797 (2015).
8. L. L. Doskolovich, D. A. Bykov, E. A. Bezus, V. A. Soifer, Spatial differentiation of optical beams using phase-shifted Bragg grating. *Opt. Lett.* **39**, 1278–1281 (2014).
9. A. Youssefi, F. Zangeneh-Nejad, S. Abdollahramezani, A. Khavasi, Analog computing by Brewster effect. *Opt. Lett.* **41**, 3467–3470 (2016).
10. D. A. Bykov, L. L. Doskolovich, E. A. Bezus, V. A. Soifer, Optical computation of the Laplace operator using phase-shifted Bragg grating. *Opt. Express* **22**, 25084–25092 (2014).
11. N. V. Golovastikov, D. A. Bykov, L. L. Doskolovich, E. A. Bezus, Spatial optical integrator based on phase-shifted Bragg gratings. *Opt. Commun.* **338**, 457–460 (2015).
12. Z. Ruan Spatial mode control of surface plasmon polariton excitation with gain medium: From spatial differentiator to integrator. *Opt. Lett.* **40**, 601–604 (2015).
13. S. AbdollahRamezani, K. Arik, A. Khavasi, Z. Kavehvash, Analog computing using graphene-based metalines. *Opt. Lett.* **40**, 5239–5242 (2015).
14. A. Chizari, S. Abdollahramezani, M. V. Jamali, J. A. Salehi, Analog optical computing based on a dielectric meta-reflect array. *Opt. Lett.* **41**, 3451–3454 (2016).
15. Y. Hwang, T. J. Davis, Optical metasurfaces for subwavelength difference operations. *Appl. Phys. Lett.* **109**, 181101 (2016).
16. T. Zhu *et al.*, Plasmonic computing of spatial differentiation. *Nat. Commun.* **8**, 15391 (2017).
17. A. Saba, M. R. Tavakol, P. Karimi-Khoozani, A. Khavasi, Two-dimensional edge detection by guided mode resonant metasurface. *IEEE Photonics Technol. Lett.* **30**, 853–856 (2018).
18. J. Goodman, *Introduction to Fourier Optics* (Roberts & Company Publishers, Englewood, CO, 2005).
19. H. Hu, C. Ma, Z. Liu, Plasmonic dark field microscopy. *Appl. Phys. Lett.* **96**, 113107 (2010).
20. S. Pancharatnam, Generalized theory of interference, and its applications. *Proc. Indian Acad. Sci. A*, **44**, 5, 398–417 (1956).
21. M. V. Berry, Quantal phase factors accompanying adiabatic changes. *Proc. R. Soc. London Ser. A*, **392**, 45–57 (1984).
22. Z. Bomzon, G. Biener, V. Kleiner, E. Hasman, Space-variant Pancharatnam-Berry phase optical elements with computer-generated subwavelength gratings. *Opt. Lett.* **27**, 1141–1143 (2002).
23. L. Huang *et al.*, Dispersionless phase discontinuities for controlling light propagation. *Nano Lett.* **12**, 5750–5755 (2012).
24. N. Shitrit, I. Bretner, Y. Gorodetski, V. Kleiner, E. Hasman, Optical spin Hall effects in plasmonic chains. *Nano Lett.* **11**, 2038–2042 (2011).
25. W. Luo, S. Xiao, Q. He, S. Sun, L. Zhou, Photonic spin Hall effect with nearly 100% efficiency. *Adv. Opt. Mater.* **3**, 1102–1108 (2015).
26. X.-G. Luo, M.-B. Pu, X. Li, X.-L. Ma, Broadband spin Hall effect of light in single nanoapertures. *Light Sci. Appl.* **6**, e16276 (2017).
27. D. Lin, P. Fan, E. Hasman, M. L. Brongersma, Dielectric gradient metasurface optical elements. *Science* **345**, 298–302 (2014).
28. X. Yin, Z. Ye, J. Rho, Y. Wang, X. Zhang, Photonic spin Hall effect at metasurfaces. *Science* **339**, 1405–1407 (2013).
29. A. Shaltout, J. Liu, A. Kildishev, V. Shalaev, Photonic spin Hall effect in gap–plasmon metasurfaces for on-chip chiroptical spectroscopy. *Optica* **2**, 860–863 (2015).
30. Y. Shimotsuma, P. G. Kazansky, J. Qiu, K. Hirao, Self-organized nanogratings in glass irradiated by ultrashort light pulses. *Phys. Rev. Lett.* **91**, 247405 (2003).
31. J. Zhou *et al.*, Broadband photonic spin Hall meta-lens. *ACS Nano* **12**, 82–88 (2018).
32. D. Hakobyan, E. Brasselet, Left-handed optical radiation torque. *Nat. Photonics* **8**, 610–614 (2014).
33. Z. Bomzon, V. Kleiner, E. Hasman, Pancharatnam–Berry phase in space-variant polarization-state manipulations with subwavelength gratings. *Opt. Lett.* **26**, 1424–1426 (2001).
34. G. Biener, A. Niv, V. Kleiner, E. Hasman, Formation of helical beams by use of Pancharatnam-Berry phase optical elements. *Opt. Lett.* **27**, 1875–1877 (2002).
35. M. D. Robinson, D. G. Stork, Joint digital-optical design of superresolution multiframe imaging systems. *Appl. Opt.* **47**, B11–B20 (2008).

Zhou et al.